

Sound speed uncertainty in Acousto-Electric Tomography

Bjørn Jensen* and Kim Knudsen†

Department of Applied Mathematics and Computer Science
 Technical University of Denmark
 2800 Kgs. Lyngby, Denmark

Abstract

The goal in acousto-electric tomography (AET) is to reconstruct an image of the unknown electric conductivity in an object from exterior electrostatic currents and voltages that are measured on the boundary of the object while the object is penetrated by propagating ultrasound waves. This problem is a coupled-physics inverse problem. Accurate knowledge of the propagating ultrasound wave is usually assumed and required, but in practice tracking the propagating wave is very hard, or potentially impossible, due to inexact knowledge of the object's interior acoustic wave speed. In this work, we model uncertainty in the wave speed, and formulate a suitable reconstruction method for the power density and conductivity. We also establish theoretical error bounds, and show that the suggested approach can be understood as a regularization scheme for the inverse problem. Finally, we simulate the wave speed from a numerical breast tissue model, and computationally explore the severity of the error in the reconstructions. Our results show that with reasonable sound speed uncertainty, reliable reconstruction is possible.

Keywords: acousto-electric tomography, electrical impedance tomography, uncertainty quantification, hybrid data tomography, variable sound speed, coupled physics imaging, inverse problems, medical imaging

MSC2000: 35R30; 65N21

1 Introduction

Acousto-electric tomography (AET) is a hybrid imaging technique combining electro-static boundary measurements as in *electrical impedance tomography* (EIT) [10, 12, 15] with an ultrasound component with the aim to provide tomographic images with much better contrast and resolution compared to images produced by EIT alone. The ultrasound wave is emitted into the object and passes through the object causing local contraction and expansion of the medium due to the acoustic pressure. The changes produce slight local volume deformations inducing a small change of conductivity and thus changing the measurements at the boundary [18, 22]; this effect is referred to as *acousto-electric interaction*, *acousto-electric modulation* or the *acousto-electric effect*. The inverse problem is then to obtain the conductivity from these wave-dependent electro-static boundary measurements.

EIT is a well established technology in medical imaging, for instance for the bedside monitoring of lung function. EIT would also make sense for cancer detection due to high contrast in the electric properties of cancerous tissue compared to healthy tissue, but the low of resolution is a great concern. A remedy can be found in hybrid imaging modalities for instance AET.

*bcsj@dtu.dk; <https://orcid.org/0000-0002-4743-2631>

†kiknu@dtu.dk; <https://orcid.org/0000-0002-4875-3074>

Our work in this paper is inspired by the use of AET for breast cancer imaging. Our studies are conceptual and computational rather than data driven, so specific parameter values are not relevant.

AET requires complete knowledge of the waves that travel through the object. This, in turn, requires complete knowledge of the object's sound speed. However, in many applications, the object's sound speed is not fully known; only a rough estimate of the magnitude is provided and can be used in the inversion framework. In breast tissue it is reasonable to model the sound speed to be constant, with variations up to 10% [26].

In this paper we focus on the following question: *To what extent can we trust power density and conductivity reconstructions in AET, when the sound speed is known up to uncertainty due to small variations.* We model numerically the uncertainty in the sound speed. Inspired by potential applications in breast cancer detection we adapt the tissue model in [27] to numerically produce such sound speed variations. We then suggest a reconstruction framework based on [17]. We show theoretically that our approach is consistent in the sense of inverse problem's regularization theory: in the limit of vanishing sound speed uncertainty we perfectly reconstruct the conductivity. Moreover, our computational framework allows us to quantify the consequence of sound speed uncertainty on the reconstructions.

AET has been studied before by a variety of authors. The method was considered experimentally in [30]. The measurements in AET have, however, a low signal-to-noise ratio, and therefore only limited experimental progress has been observed since. The problem is well-understood theoretically [5, 7, 8, 11, 20, 21, 25]. Numerical algorithms have been discussed in [2, 3, 6, 23, 28], and [16] studies the problem with limited boundary access. Also, for a survey of theory for inverse problem pertaining to both AET and related problems, see the book [4]. While to the best of our knowledge AET has not seen any study related to uncertainty quantification prior to this work, we should mention that there is some work on the unknown sound speed problem [26, 29] for related hybrid problems *photoacoustic tomography* (PAT) and *thermoacoustic tomography* (TAT) .

The outline of this paper is as follows. In Section 2 we describe the AET model, including the sound speed modeling. In Section 3 we obtain continuity results for the AET data with respect to the sound speed variations. In Section 4 we recall the optimization problem formulations of the involved inverse problems; first recovery of the power density and from there recovery of the conductivity. We go on to prove that our approach forms a proper regularization strategy for the model error. In Section 5 we describe the numerical implementation of the forward models. We also describe the procedure used for sampling random sound speed with structures for our numerical computations. In section 6 we show reconstructions and describe the numerical results, and Section 7 contains discussion and concluding remarks.

2 Modeling acousto-electric tomography

The modeling of AET follows [17]. In \mathbb{R}^d , $d = 2, 3$, an ultrasound wave generated by a source $S(x, t)$ is modelled by the scalar wave equation

$$\begin{cases} (\partial_t^2 - c^2 \Delta) p = S & \text{in } \mathbb{R}^d \times \mathbb{R}_+, \\ p|_{t=0} = \partial_t p|_{t=0} = 0 & \text{on } \mathbb{R}^d, \end{cases} \quad (2.1)$$

where $c(x)$ is the spatially dependent *sound speed*. We assume that the source S is fully known, smooth and compactly supported, and that $c \in C^\infty(\mathbb{R}^d)$ is bounded, and bounded from below, by a positive constant. Then (2.1) has a unique weak solution, see e.g. [13, Sec. 7.2].

The electric conductivity is modeled by a real-valued function σ in a bounded and open subset $\Omega \subset \mathbb{R}^d$ with smooth boundary $\partial\Omega$. The function σ belongs to $L^\infty(\Omega)$ and is bounded from below by a positive constant. When a current flux f is applied on $\partial\Omega$, an electric potential

u is generated in Ω , and assuming no interior sources or sinks of charge, the electrical potential u satisfies the partial differential equation (PDE)

$$\begin{cases} -\nabla \cdot \sigma \nabla u = 0 & \text{in } \Omega, \\ \sigma \partial_\nu u = f & \text{on } \partial\Omega. \end{cases} \quad (2.2)$$

The vector ν denotes the outward pointing unit normal on $\partial\Omega$ and $\sigma \partial_\nu u = \nu \cdot \sigma \nabla u$ is the normal component of the current field $J = \sigma \nabla u$. The compatibility condition $f \in L^2_\diamond(\partial\Omega) = \{v \in L^2(\partial\Omega) : \int_{\partial\Omega} v \, ds = 0\}$ (corresponding to conservation of charge) guarantees that (2.2) has a weak solution $u \in H^1(\Omega)$ unique up to a constant, which is fixed by requiring $g = u|_{\partial\Omega} \in L^2_\diamond(\partial\Omega)$ [13].

When the wave p propagates through Ω , the conductivity is perturbed due the acousto-electric effect. The perturbed conductivity $\sigma_*(x, t)$ is described by the first order model

$$\sigma_* = \sigma(1 + \eta p), \quad (2.3)$$

where $\eta > 0$ is called the acousto-electric coupling constant and is assumed to be known.

Substituting σ_* for σ in (2.2) yields the PDE

$$\begin{cases} -\nabla \cdot (\sigma_* \nabla u_*) = 0 & \text{in } \Omega, \\ \sigma_* \partial_\nu u_* = f & \text{on } \partial\Omega. \end{cases} \quad (2.4)$$

characterizing for fixed $t \in \mathbb{R}_+$ the resulting time-dependent electrical potential $u_*(x, t)$. For uniqueness, we again fix the constant so $g_*(\cdot, t) = u_*|_{\partial\Omega}(\cdot, t) \in L^2_\diamond(\partial\Omega)$.

The inverse problem of AET is now to reconstruct σ from knowledge of several triplets (f, g, g_*) corresponding to different choices of f . Integrating f and $g_* - g$ along the boundary defines the time signal

$$I(t) = \int_{\partial\Omega} f(g_*(\cdot, t) - g) \, dS$$

The function $I(t)$ is the time evolution of the difference in power for the system under the influence of the wave perturbation. We assume $I(t)$ is known for $t \in (0, T)$ for some sufficiently large $T > 0$. An example of $I(t)$ is shown in Figure 1. The blue curve illustrates $I(t)$ for the depicted conductivity phantom with a circular inclusion. The gray curve is for reference $I(t)$ for a homogeneous conductivity. Using the function I , we can now pose the inverse problem of AET as follows: Given I for several boundary conditions f and wave sources S , reconstruct the conductivity σ . Note that, in the reduction of the different electric boundary signals (f, g, g_*) to the time signal I , we could consider cross-terms by integrating f to a $g - g_*$ coming from a different boundary current. This might stabilize the problem. Instead we use more boundary conditions.

In solving the inverse problem, the crucial intermediate object is the interior power density $H(x)$, $x \in \Omega$, for (2.2) given by

$$H = \sigma |\nabla u|^2. \quad (2.5)$$

where $u = u[\sigma]$ is the solution of (2.2). The power density shows up by considering the weak forms of (2.2) and (2.4), each with the solution of the other taken as a test function therein. Taking their difference and approximating $u_* \approx u$ gives

$$I = -\eta \int_{\Omega} p \sigma \nabla u \cdot \nabla u_* \, dx \quad (2.6)$$

$$\approx -\eta \int_{\Omega} p \overbrace{\sigma |\nabla u|^2}^H \, dx. \quad (2.7)$$

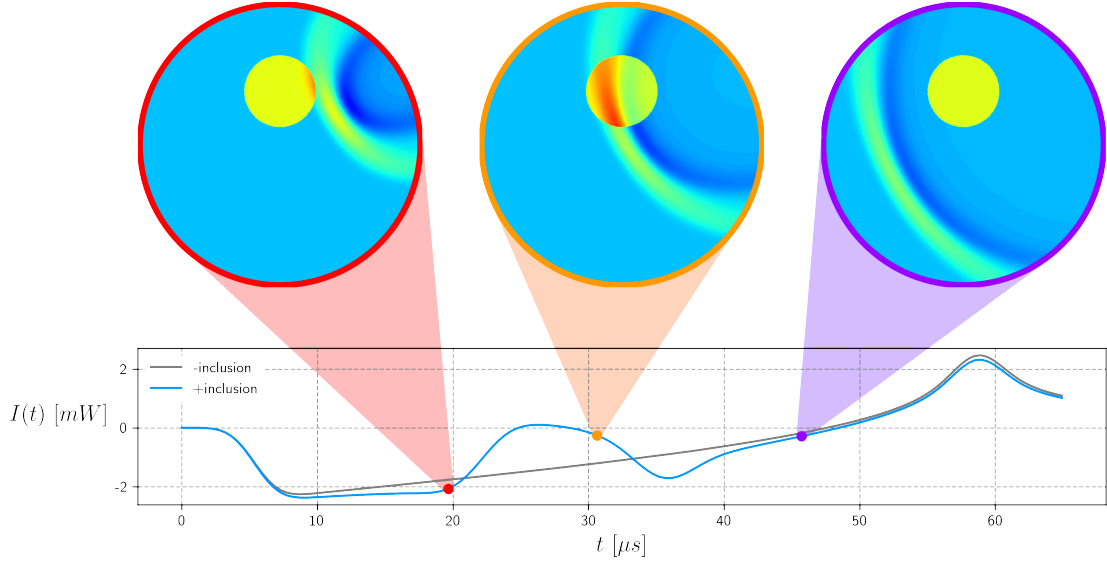


Figure 1: Upper plot shows the perturbed conductivity σ_* due to propagating acoustic wave at key times. The lower plot shows the time signal $I(t)$ for the conductivity phantom with a circular inclusion (blue) and for a homogeneous reference (gray).

We thus pose the linear inverse problem to find H from the equation

$$I = KH \quad (2.8)$$

with K denoting the integral operator with kernel $-\eta p$

$$KH(t) = -\eta \int_{\Omega} p(x, t) H(x) dx. \quad (2.9)$$

Since $p \in L^2(\Omega \times (0, T))$, the operator $K : L^2(\Omega) \rightarrow L^2(0, T)$ is compact.

The inverse problem is now first to recover the power density H by solving (2.8); then to recover σ from several H corresponding to different choices of f .

Remark 2.1. Equations (2.8)–(2.9) illustrate the importance of $p(x, t)$ in the reconstruction, and how, ideally, $\{p(\cdot, t)\}_{t \in (0, T)}$ should constitute a complete set in $L^2(\Omega)$ for $H(x)$ to be fully determined. In this sense, if the set is not complete, the best we may hope to reconstruct is the projection of $H(x)$ to the subspace of $L^2(\Omega)$ spanned by the waves.

There are in general multiple possible sources of errors in AET. The most obvious include measurement errors, linearization errors, and model errors. In this work we are interested in exploring the effect of uncertainty in the sound speed c . We do so by considering the sound speed to be unknown to us. Instead, we assume prior knowledge of the mean value of the sound speed in the reconstruction approach. Using a wrong sound speed corresponds to having a model error.

We consider sound speeds c and \tilde{c} , where the former represents the true sound speed and the latter an approximation due to prior knowledge. Numerically, we model c by

$$c(x) = c_{\text{bg}} + c_{\text{var}}(x),$$

where c_{var} , carries information about the uncertainty in c due to variations in tissue and due to inclusions in the phantom. We take $\tilde{c} = c_{\text{bg}}$ constant in our studies.

3 Stability of the forward operator

In this section, we demonstrate that, under certain assumptions, the wave p and forward operator K are continuously dependent on the sound speed c . This guarantees that errors in the data are controlled by errors in the sound speed. The results are likely well-known, but with the lack of a proper reference, we indicate the overall ideas.

Let $m = \lceil \frac{d+1}{2} \rceil$. We define the admissible set of sound speeds as the set of smooth functions bounded from above and below by positive constant $\lambda \in (0, 1)$

$$\mathcal{A}_\lambda := \{c \in C^\infty(\mathbb{R}^d) : \lambda \leq c \leq \lambda^{-1}; \|c\|_{C^k(\mathbb{R}^d)} < \lambda^{-1}, k \leq m+1\}.$$

A positive lower bound on c ensures that $\partial_t^2 - c^2 \Delta$ is a uniformly hyperbolic operator. The upper bound yields finite propagation speed for the wave p [13]; the bound on C^k norms allow uniform estimates inside \mathcal{A}_λ . We assume in the following that λ is fixed and that $c, \tilde{c} \in \mathcal{A}_\lambda$.

Put $h = \tilde{c} - c$ and $q = \tilde{p} - p$. Clearly q solves the PDE

$$\begin{cases} (\partial_t^2 - \tilde{c}^2 \Delta) q = h(\tilde{c} + c)\Delta p, & \text{in } \mathbb{R}^d \times \mathbb{R}_+, \\ q|_{t=0} = \partial_t q|_{t=0} = 0, & \text{on } \mathbb{R}^d. \end{cases} \quad (3.1)$$

Note that, due to the finite speed of propagation, $\text{supp}\{h(\tilde{c} + c)\Delta p(\cdot, t)\}$ is compact and so is the support of q . We denote by $B \subset \mathbb{R}^d$ a large ball that contains the support of both $h(\tilde{c} + c)\Delta p$ and q for all $t \in (0, T)$. For all m , the regularity of q can now be estimated [13, p.415] by

$$\text{ess sup}_{0 \leq t \leq T} \sum_{j=0}^{m+1} \left\| \partial_t^j q(\cdot, t) \right\|_{H^{m+1-j}(B)} \leq C \sum_{j=0}^m \left\| h(\tilde{c} + c)\Delta \partial_t^j p \right\|_{L^2(0, T; H^{m-j}(B))}, \quad (3.2)$$

where C depends on the C^{m+1} -norm of c ; thus by $c \in \mathcal{A}_\lambda$ it depends only on λ . This leads to:

Proposition 3.1.

$$\|\tilde{p} - p\|_{L^\infty(0, T; H^{m+1}(B))} \leq C \|\tilde{c} - c\|_{H^m(B)}, \quad (3.3)$$

where C does not depend on \tilde{c} .

Proof. Observe that, for any positive index k , $\|\cdot\|_{L^2(0, T; H^{m-k}(B))} \leq \|\cdot\|_{L^2(0, T; H^m(B))}$, and moreover that for $m > d/2$, $H^m(\omega)$ is a Banach algebra [1, 4.39]. Applying these observations to (3.2) yield

$$\|\tilde{p} - p\|_{L^\infty(0, T; H^{m+1}(B))} \leq C \|\tilde{c} - c\|_{H^m(B)} \sum_{k=0}^m \|\tilde{c} + c\|_{L^2(0, T; H^m(B))} \|\Delta \partial_t^k p\|_{L^2(0, T; H^m(B))},$$

for some $C > 0$. Since $\tilde{c} + c \leq 2\lambda^{-1}$ and $p \in C^\infty$ we get (3.3). \square

Remark 3.1. By boundedness of Ω we can without loss of generality assume $\Omega \subseteq B$.

The established continuity for the wave upon the sound speed yields operator continuity for the forward operator in the following sense.

Proposition 3.2. *The operator difference $\tilde{K} - K: L^2(\Omega) \rightarrow L^2(0, T)$ is bounded by*

$$\|\tilde{K} - K\| \leq C \|\tilde{c} - c\|_{H^m(B)},$$

where C does not depend on \tilde{c} .

Proof. By the Cauchy-inequality

$$\frac{\|(\tilde{K} - K)H\|_{L^2(0, T)}^2}{\|H\|_{L^2(\Omega)}^2} = \frac{\eta^2 \int_0^T [\int_\Omega (\tilde{p} - p)H \, dx]^2 dt}{\|H\|_{L^2(\Omega)}^2} \leq \eta^2 T \|\tilde{p} - p\|_{L^\infty(0, T; L^2(\Omega))}^2,$$

which shows $\|\tilde{K} - K\| \leq \eta\sqrt{T} \|\tilde{p} - p\|_{L^\infty(0, T; L^2(\Omega))}$. Proposition 3.1 now gives the estimate. \square

4 Inversion procedure

In this section, we introduce the applied inversion procedure. The problem is dealt with in two parts, both handled as regularized minimization problems. Firstly, the power densities are reconstructed from the measured differences in power consumption $I(t)$ by a standard least-squares approach, and secondly, the conductivity is reconstructed from the recovered power densities. We elaborate on the details in our approach below.

4.1 Reconstruction of the power density

As in [17], we invert equation (2.8) by a least squares approach. In particular we consider the following Tikhonov-regularized problem, which we will discretize.

$$\arg \min_{h \in L^2(\Omega)} \frac{1}{2} \|Kh - I\|_{L^2(0,T)}^2 + \frac{\beta}{2} \|h\|_{L^2(\Omega)}^2. \quad (4.1)$$

In contrast to [17], we discretize (4.1) using a finite element basis $\{\phi_j\}_{1 \leq j \leq N}$. The regularization term is then approximated by

$$\|\mathbf{L}^T \mathbf{v}\|_2^2 = \|\mathbf{v}\|_{\mathbf{M}}^2 \approx \|v\|_{L^2(\Omega)}^2,$$

where $\mathbf{M} = \mathbf{L}\mathbf{L}^T$ is the mass matrix for the finite element basis, \mathbf{L} the Cholesky factor of \mathbf{M} , \mathbf{v} is the coefficient vector for the finite element discretization of the continuous function $v(x)$, and $\|\cdot\|_2$ is the usual Euclidean 2-norm. Thus, the finite dimensional regularized least squares problem takes the form

$$\hat{\mathbf{h}}_\beta = \arg \min_{\mathbf{h} \in \mathbb{R}^N} \frac{1}{2} \|\mathbf{K}\mathbf{h} - \mathbf{I}\|_2^2 + \frac{\beta}{2} \|\mathbf{L}^T \mathbf{h}\|_2^2, \quad (4.2)$$

where \mathbf{K} is the discretization of the operator K in (2.8). \mathbf{K} has the form

$$(\mathbf{K})_{ij} = -\eta \int_{\Omega} p(\cdot, t_i) \phi_j \, dx,$$

with $\{t_i\}_{0 \leq i \leq m}$ a uniform time-discretization; i.e. $0 = t_0 < t_1 < \dots < t_m = T$ and $t_i - t_{i-1} = \Delta t$ for all $1 \leq i \leq m$. Because the time-discretizing is uniform we may neglect the scaling coefficient, which would appear from discretizing the $L^2(0, T)$ -norm.

Remark 4.1. *To eliminate effects not relevant to our study, here we will always use the optimal β parameter in our simulations; i.e. we find an optimal $\hat{\mathbf{h}}_{\beta^*}$ by solving $\beta^* = \arg \min_{\beta \in \mathbb{R}_+} \|\hat{\mathbf{h}}_\beta - \mathbf{h}^*\|_M$, where \mathbf{h}^* is the coefficient vector for the finite element discretization of the true $H(x)$.*

4.2 Reconstruction of the conductivity

To reconstruct the conductivity from the formerly reconstructed power density, here denoted by z , we consider the following L^1 -TV optimization problem to be minimized

$$\arg \min_{\sigma} \|H[\sigma] - z\|_{L^1(\Omega)} + \gamma |\sigma|_{\text{TV}}, \quad (4.3)$$

with an $L^1(\Omega)$ data fidelity term and total variation regularization. We denote the functional in (4.3) by $\mathcal{J}(\sigma)$. For simplicity of the formulation, we consider the theory for only one power density, however the problem extends naturally to multiple by summing separate data fidelity terms. A minimizer is known to exist for this problem [2]. Our approach here will be similar to that of [2, 17], though we make certain small changes which allow us to speed up the computational performance significantly; in particular we draw inspiration from [14].

Take the linearization $H[\sigma + \kappa] \approx H[\sigma] + H'[\sigma, \kappa]$, where $H'[\sigma, \kappa] = \kappa|\nabla u[\sigma]|^2 + 2\sigma\nabla u[\sigma] \cdot \nabla u'[\sigma, \kappa]$ and $u'[\sigma, \kappa]$ is the Fréchet derivative of $u[\sigma]$ in direction κ (e.g. see [2]), and consider the following weighted quadratic functional

$$\mathcal{J}_\sigma(\kappa) = \frac{1}{2} \int_{\Omega} w[\sigma] |H'[\sigma, \kappa] - z_\sigma|^2 dx + \frac{\gamma}{2} \int_{\Omega} w_0[\sigma] |\nabla(\sigma + \kappa)|^2 dx, \quad (4.4)$$

where $w[\sigma] = |H[\sigma] - z|^{-1}$, $z_\sigma = z - H[\sigma]$ and $w_0[\sigma] = |\nabla\sigma|^{-1}$ and the absolute values $|\cdot|$ are smoothened close to zero, i.e. $|\cdot| \approx \sqrt{|\cdot|^2 + \tau^2}$ for a small $\tau > 0$. Essentially this originates from considering $\mathcal{J}(\sigma + \kappa)$, substituting the linearization of H into (4.3) and approximating the norms by weighted L^2 -norms. Instead of tackling (4.3), we take steps by iteratively minimizing (4.4) and then updating σ and computing the new weights.

Discretizing (4.4), we obtain the quadratic

$$J_\sigma(\kappa) = \frac{1}{2} \kappa^T (\mathbf{W}^T \mathbf{M}_w \mathbf{W} + \gamma \mathbf{K}_{w_0}) \kappa - \kappa^T (\mathbf{W}^T \mathbf{M}_w \mathbf{z}_\sigma - \gamma \mathbf{K}_{w_0} \sigma) + \text{constant}, \quad (4.5)$$

where, with $\{\phi_j\}_{1 \leq j \leq n}$ a finite element basis, $(\mathbf{M}_w)_{ij} = \int_{\Omega} w[\sigma] \phi_i \phi_j dx$, $(\mathbf{K}_{w_0})_{ij} = \int_{\Omega} w_0[\sigma] \phi_i \phi_j dx$ and \mathbf{W} is the discretization of the linear map $\kappa \mapsto H'[\sigma, \kappa]$. This discretization is given by $\mathbf{W} = \mathbf{M}^{-1} (\mathbf{M}_u - 2\mathbf{W}_{\sigma,u} \mathbf{K}_\sigma^{-1} \mathbf{L}_u)$, where

$$\begin{aligned} (\mathbf{M})_{ij} &= \int_{\Omega} \phi_i \phi_j dx, & (\mathbf{M}_u)_{ij} &= \int_{\Omega} |\nabla u[\sigma]|^2 \phi_i \phi_j dx, & (\mathbf{W}_{\sigma,u})_{ij} &= \int_{\Omega} \phi_i \sigma \nabla u[\sigma] \cdot \nabla \phi_j dx, \\ (\mathbf{K}_\sigma)_{ij} &= \int_{\Omega} \sigma \nabla \phi_i \cdot \nabla \phi_j dx, & \text{and} & & (\mathbf{L}_u)_{ij} &= \int_{\Omega} \phi_j \nabla u[\sigma] \cdot \nabla \phi_i dx. \end{aligned}$$

The minimization of (4.5) has the first order optimality condition

$$(\mathbf{W}^T \mathbf{M}_w \mathbf{W} + \gamma \mathbf{K}_{w_0}) \kappa = \mathbf{W}^T \mathbf{M}_w \mathbf{z}_\sigma - \gamma \mathbf{K}_{w_0} \sigma.$$

Following the idea in [14], we consider the approximation $\mathbf{K}_{w_0} \approx \mathbf{K}_{w_0} + \epsilon I$ for a small $\epsilon > 0$ allowing the Cholesky factorization $\mathbf{K}_{w_0} = \mathbf{L}_0 \mathbf{L}_0^T$, thus yielding

$$(\mathbf{L}_0^{-1} \mathbf{W}^T \mathbf{M}_w \mathbf{W} \mathbf{L}_0^{-T} + \gamma I) \tilde{\kappa} = \mathbf{L}_0^{-1} \mathbf{W}^T \mathbf{M}_w \mathbf{z}_\sigma - \gamma \mathbf{L}_0^T \sigma,$$

where $\tilde{\kappa} = \mathbf{L}_0^T \kappa$. Setting $\gamma = 0$ we obtain the preconditioned linear problem

$$\mathbf{L}_0^{-1} \mathbf{W}^T \mathbf{M}_w \mathbf{W} \mathbf{L}_0^{-T} \tilde{\kappa} = \mathbf{L}_0^{-1} \mathbf{W}^T \mathbf{M}_w \mathbf{z}_\sigma. \quad (4.6)$$

We thus minimize (4.5) by solving (4.6), with a preconditioned conjugate gradient algorithm [9, p.15]. With this we need only the evaluation of $\mathbf{K}_{w_0} = \mathbf{L}_0 \mathbf{L}_0^T$, so in practice we will neither need to compute the Cholesky factor nor the inverse of said factor.

4.3 Regularization strategy

Our aim is to solve (4.1), but since we don't have access to the true operator K but rather an approximate operator K^δ , we wish to consider a regularization strategy for the power density reconstruction such that the regularized solution approaches the true solution appropriately as the error vanishes. The novelty in our approach below compared to traditional sources on the topic, like [19, Sec. 2], is that in our considerations here the error appears in the operator rather than as noise in the measurements.

Let V and W be Hilbert spaces and $K, K^\delta : W \rightarrow V$ operators. Suppose $I = KH$, where K corresponds to some true sound speed c and consider K^δ coming from an approximate sound speed c^δ , such that $\|K - K^\delta\| < \delta$. We first note that $\|((K^\delta)^* K^\delta + \beta \mathcal{I})^{-1}\| \leq \beta^{-1}$, i.e independent of δ , by

$$\beta \|w\|_W^2 \leq \beta \|w\|_W^2 + \|K^\delta w\|_V^2 = \langle w, ((K^\delta)^* K^\delta + \beta \mathcal{I}) w \rangle_W \leq \|w\|_W \|((K^\delta)^* K^\delta + \beta \mathcal{I}) w\|_W.$$

Define $R_\beta^\delta = ((K^\delta)^* K^\delta + \beta \mathcal{I})^{-1} (K^\delta)^*$ and let $w^\delta = ((K^\delta)^* K^\delta + \beta \mathcal{I})^{-1} z$, then

$$\begin{aligned} \|(R_\beta^\delta)^* z\|_V^2 &= \left\langle K^\delta [((K^\delta)^* K^\delta + \beta \mathcal{I})^{-1}]^* z, K^\delta [((K^\delta)^* K^\delta + \beta \mathcal{I})^{-1}]^* z \right\rangle_V = \langle w^\delta, (K^\delta)^* K^\delta w^\delta \rangle_W \\ &\leq \langle w^\delta, (K^\delta)^* K^\delta w^\delta \rangle_W + \beta \langle w^\delta, w^\delta \rangle_W = \langle w^\delta, z \rangle_W \leq \|w^\delta\|_W \|z\|_W \leq \beta^{-1} \|z\|_W^2, \end{aligned}$$

thus $\|(R_\beta^\delta)^*\| = \|R_\beta^\delta\| \leq \beta^{-\frac{1}{2}}$. Assume there is a \bar{w} satisfying $K^* \bar{w} = H$ then

$$\begin{aligned} \|H - R_\beta^\delta I\|_W &= \|H - ((K^\delta)^* K^\delta + \beta \mathcal{I})^{-1} (K^\delta)^* K H\|_W \\ &= \|((K^\delta)^* K^\delta + \beta \mathcal{I})^{-1} [(K^\delta)^* K^\delta + \beta \mathcal{I} - (K^\delta)^* K] H\|_W \\ &= \|R_\beta^\delta [K^\delta - K] H + \beta ((K^\delta)^* K^\delta + \beta \mathcal{I})^{-1} H\|_W \\ &= \|R_\beta^\delta [K^\delta - K] H + \beta ((K^\delta)^* K^\delta + \beta \mathcal{I})^{-1} ((K^\delta)^* + K^* - (K^\delta)^*) \bar{w}\|_W \\ &= \|R_\beta^\delta [K^\delta - K] H + \beta R_\beta^\delta \bar{w} + \beta ((K^\delta)^* K^\delta + \beta \mathcal{I})^{-1} (K^* - (K^\delta)^*) \bar{w}\|_W \\ &\leq \|R_\beta^\delta\| \underbrace{\|K^\delta H - K H\|_V}_{\leq \|K^\delta - K\| \|H\|_W < \delta \|H\|_W} + \beta \|R_\beta^\delta\| \|\bar{w}\|_V + \beta \underbrace{\|((K^\delta)^* K^\delta + \beta \mathcal{I})^{-1} (K^* - (K^\delta)^*) \bar{w}\|_W}_{\leq \beta^{-1} \|K^* - (K^\delta)^*\| \|\bar{w}\|_V \leq \beta^{-1} \delta \|\bar{w}\|_V} \\ &\leq \frac{\delta}{\sqrt{\beta}} \|H\|_W + \sqrt{\beta} \|\bar{w}\|_V + \delta \|\bar{w}\|_V. \end{aligned}$$

Thus $H^{\beta, \delta} \equiv R_\beta^\delta I \rightarrow H$ as $\beta \rightarrow 0$ and $\delta \rightarrow 0$ together. It is an easy extension to also consider noise in I . We summarize in the following theorem.

Theorem 4.1. *Let K and K^δ satisfy $\|K - K^\delta\| < \delta$ and $I = KH$ with $\|I - I^\varepsilon\| < \varepsilon$. If there exists \bar{w} satisfying $K^* \bar{w} = H$ and $\delta/\sqrt{\beta(\delta, \varepsilon)} \rightarrow 0$, $\varepsilon/\sqrt{\beta(\delta, \varepsilon)} \rightarrow 0$ and $\beta(\delta, \varepsilon) \rightarrow 0$ as $\delta, \varepsilon \rightarrow 0$, then*

$$\|H - R_\beta^\delta I^\varepsilon\|_W \rightarrow 0 \quad \text{as } \delta, \varepsilon \rightarrow 0,$$

where $R_\beta^\delta = ((K^\delta)^* K^\delta + \beta \mathcal{I})^{-1} (K^\delta)^*$; i.e. R_β^δ is a regularization strategy.

Remark 4.2. *Assume for instance that $\delta \propto \varepsilon^\alpha$, $\alpha > 0$, asymptotically as they vanish, then $\beta(\delta, \varepsilon) = \delta^a \varepsilon^b$, where $0 < a, b < 2$ solves $\frac{2-a}{b} > \alpha$ and $\alpha > \frac{a}{2-b}$, works. For simplicity, taking $a = b = \frac{1}{k}$ all $k > \frac{\alpha+1}{2}$ are solutions.*

The following corollary is a direct consequence of combining the above derivations with Propositions 3.1 and 3.2 from Section 3.

Corollary 4.1. *Assume that m, c, \tilde{c}, K and \tilde{K} are as in Section 3, that $I = KH$ and that $H \in \text{Ran}(K^*)$. If $\beta \propto \|\tilde{c} - c\|_{H^m(B)}$ there is a constant $C > 0$ independent of \tilde{c} and β such that*

$$\|H - R_\beta I\|_{L^2(\Omega)} \leq C \|\tilde{c} - c\|_{H^m(B)}^{\frac{1}{2}},$$

where $R_\beta = (\tilde{K}^* \tilde{K} + \beta \mathcal{I})^{-1} \tilde{K}^*$.

This demonstrates that, as the sound speed \tilde{c} converges to c , and the regularization vanishes appropriately relative to each other, the solution of (4.1), with operator \tilde{K} , converges to the true solution H .

5 Numerical implementation and uncertainty modeling

Simulations are done in 2d. In general we follow the approach in [17, Sec. 3.3] though with some deviations. In the subsections we sketch our approach.

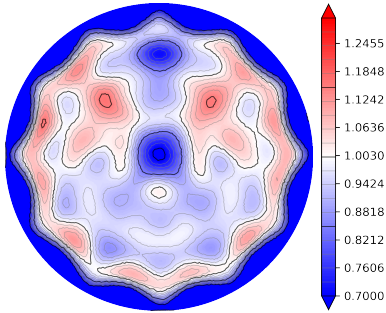


Figure 2: Reconstruction of $H(x)$ for boundary condition $f(x, y) = y$ and 12 uniformly distributed wave sources. This reconstruction is done using a forward model with a homogeneous sound speed c from data generated with a homogeneous sound speed $\tilde{c} = 1.05c$. This illustrates star-like shape artifacts resulting from having few waves, and the low-energy band close to the boundary resulting from the severely wrong mean sound speed assumption (here too low).

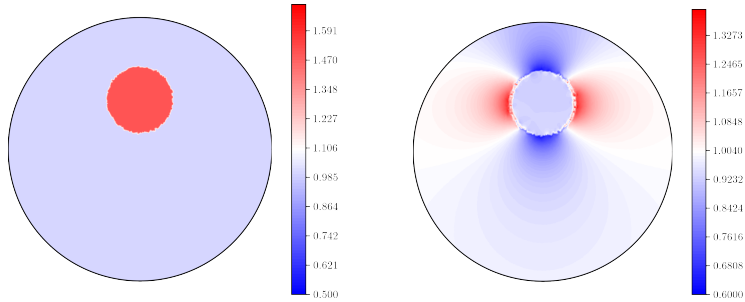


Figure 3: The true conductivity $\sigma_{\text{true}}(x)$ on the left and the directly computed power density $H(x)$ corresponding to the boundary condition $f(x_1, x_2) = x_1$.

5.1 Forward models

We solve the wave equation (2.1) using the K-WAVE package for MATLAB. This is done on a regular square grid in a domain $[-L, L]^2 \subset \mathbb{R}^2$ and, to simulate the full domain \mathbb{R}^2 , an absorbing boundary layer is added such that from within the subdomain $[-L', L']^2 \subset [-L, L]^2$ the solution is an approximation to the problem in the full space. Note that the domain of our electrical measurements Ω is contained in $[-L', L']^2$.

The sound speed c is generated based on a breast tissue model [27]. The model along with the changes introduced to accommodate our problem are outlined in Section 5.2. The wave speed for generating the data has the form

$$c(x) = (c_{\text{bg}} + \chi_D(x)(c_{\text{incl}} - c_{\text{bg}}))(1 + \mu s(x)), \quad (5.1)$$

where $s(x)$ is a sampled structured perturbation and μ is a small scaling factor; we take $\mu = 0.05$ in our simulations unless otherwise specified. $c_{\text{bg}} = 1500$ and $c_{\text{incl}} = 1650$ are the background and inclusion sound speeds respectively. $\chi_D(x)$ denotes the indicator function on $D = B_{\frac{1}{4}}(0, \frac{3}{8})$.

We use 36 uniformly distributed wave-source positions in order to eliminate artifacts related to a limited number of waves; see Figure 2. Each transducer source consists of a sequence of point sources on the arc of $\partial\Omega$, whereas in [17] the point sources lie on a straight line tangential to $\partial\Omega$; we note that the choice, when consistent in the modeling, is not significant. Also, at each transducer source position, we have only one steering angle directed radially inwards.

The generated acoustics fields, all captured in $p(x, t)$, are interpolated on an unstructured triangulated mesh \mathcal{M} with 20100 nodes.

The electrical potentials are computed as in [17] using FENICS [24] with a \mathcal{P}_1 finite element basis on the mesh \mathcal{M} . To ensure no other sources of uncertainty than the unknown sound speed, no noise components are added at this step. Moreover, we avoid the linearization error (2.6)–(2.7) by generating our time series data directly by first forming the power density H , and then by integrating numerically in the linear expression (2.7).

The conductivity phantom is $\sigma_{\text{true}}(x) = 1 + \frac{1}{2}\chi_D(x)$. Figure 3 illustrates σ together with the directly computed power density $H(x)$ corresponding to the boundary condition $f(x_1, x_2) = x_1$. We show the power density to illustrate what would be the ideal reconstruction from the first step.

5.2 Noise sampling scheme

We sample different structures for the sound speed c and generate data to observe the influence on the reconstructions. The sound speed is sampled as follows: We consider a slightly modified 2D version of the breast tissue model proposed in [27]. Our approach is summarized here to make apparent the different choices.

Firstly, we define constants $f_0 = 20$, $\ell = 25$, $c_0 = 0.5$, $c_1 = 1$ and an $N \times N$ -grid with points $\xi_{jk} := (\xi_j, \xi_k) \in [-\ell, \ell]^2$, $1 \leq j, k \leq N$, $\xi_j = \ell \left(2 \frac{j-1}{N-1} - 1\right)$. Secondly, we draw uniformly distributed phase samples for each node in the grid, $\theta_{jk} \sim \mathcal{U}(-\pi, \pi)$. We define the function $V_\beta(\xi; \theta)$, as

$$V_\beta(\xi; \theta) = \begin{cases} c_0, & |\xi| = 0, \\ c_1 |\xi|^{-\frac{\beta}{2}} e^{-i\theta}, & 0 < |\xi| < f_0, \\ 0, & \text{otherwise,} \end{cases} \quad (5.2)$$

and evaluate at each grid point, $v_{jk} = V_\beta(\xi_{jk}; \theta_{jk})$. We take the discrete inverse 2D Fourier transform of v_{jk} , thus defining $q_{jk} = |\mathcal{F}_{\text{discrete}}^{-1} v_{jk}|$. Define a region $U \subseteq [-\ell, \ell]^2$, where we want to control the structures, and let $\mathcal{J} = \{(j, k) : (\xi_j, \xi_k) \in U\}$ and

$$r(\gamma) := \arg \min_{r \in \mathbb{R}} \left| \gamma - \frac{1}{|\mathcal{J}|} \sum_{(j,k) \in \mathcal{J}} \max(\text{sign}(r - q_{jk}), 0) \right|.$$

That is, $r(\gamma)$ is the height at which to make a cut such that the ratio of grid points in U with values less than $r(\gamma)$ compared to the total amount of grid points in U is as close to γ as possible. We then put

$$\hat{q}_{jk} = \begin{cases} 1 & \text{if } q_{jk} < r(\gamma), \\ 0 & \text{otherwise.} \end{cases}$$

We thus have a random (due to sampling of θ_{ij}) map $(\beta, \gamma) \mapsto \hat{Q}_{jk}(\beta, \gamma) := \hat{q}_{jk}$. From here we take some liberties in constructing our random structured sound speed. We proceed as follows: Define $\beta_0 = 3.3$, $\beta_1 = 2.8$ and $\gamma = 0.35$ (we comment on the choice of U in Remark 5.2) and let

$$s_{jk} := Q_{jk}(\beta_0, \gamma) - Q_{jk}(\beta_1, \gamma).$$

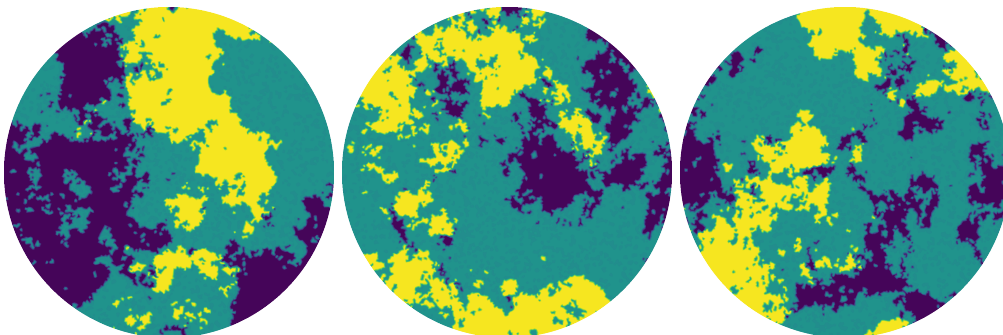


Figure 4: Examples of draws from $s(x; \theta)$; (■, ■, ■) = (1, 0, -1).

Note that s_{jk} takes only the discrete values -1, 0 and 1. We define $s(x; \theta)$ as the linear grid interpolation of s_{jk} . With the stochastic quantity s in place, $c(x) = c(x; \theta)$ in (5.1) is now a random function.

Remark 5.1. Note that a sampled $c(x; \theta)$ may have a mean speed in its domain slightly different from c_{bg} . Since the range of s_{jk} is discrete, $c(x; \theta)$ may have very steep areas depending on the grid. A smoothed version may be obtained by convolution with a mollifier.

Remark 5.2. We choose $U \subset \Omega$ slightly away from the boundary of Ω , U is here a disc with radius 0.8 times the radius of Ω , to ensure that the primary amount of variations will be exhibited in the central part of Ω .

Remark 5.3. Furthermore, we scale the domain on which $c(x; \theta)$ is defined to coincide with the square domain we have for wave equation. In this sense, the choice of value for ℓ in the sampling scheme is arbitrary and we could scale everything relative to a different choice; e.g. let $\alpha > 0$ and consider a new $\ell \rightarrow \alpha\ell$, then we should use $f_0 \rightarrow \alpha f_0$ and scale $|\xi| \rightarrow |\xi/\alpha|$ in $V_\beta(\xi; \theta)$ to compensate.

5.3 Sampling statistics

By sampling from $c(x; \theta)$ and applying the modeling sequence to compute $p(x, t; \theta)$ via (2.1), $\sigma_*(x, t; \theta)$ via (2.3) and $u_*(x, t; \theta)$ via (2.4), by (2.6) we end up with the simulated data samples $I(t; \theta)$.

Sampling $I(t; \theta)$ let $X_j(\theta) = I(t_j; \theta)$ and $x_j^1, x_j^2, \dots, x_j^n$ be samples from X_j and \bar{x}_j and x_j^σ be respectively the average and the standard deviation of those samples. The covariance and correlation matrices are $(\Gamma_{cov})_{ij} = \text{cov}(X_i, X_j)$ and $(\Gamma_{corr})_{ij} = \text{corr}(X_i, X_j) = (x_i^\sigma x_j^\sigma)^{-1} (\Gamma_{cov})_{ij}$. The covariance matrix may be approximated by the sampled covariance matrix,

$$\text{cov}(X_i, X_j) \approx (\Gamma_{cov, \text{samp}})_{ij} = \frac{1}{n-1} \sum_{k=1}^n (x_i^k - \bar{x}_i)(x_j^k - \bar{x}_j).$$

As can be seen in Figures 5 and 6 clearly there is a lot of structure to the (sampled) correlation matrix.

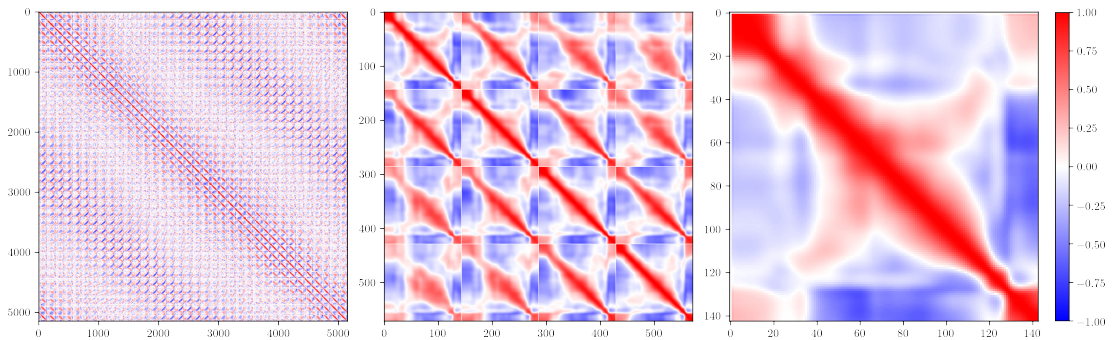


Figure 5: The (sampled) correlation matrix Γ_{corr} for $I(t_i; \theta)$; 150 samples. From left to right: left) The full correlation matrix, center) the upper left 4-by-4 blocks corresponding to 4 different wave sources, and right) the upper left first block corresponding to a single wave's correlation with itself.

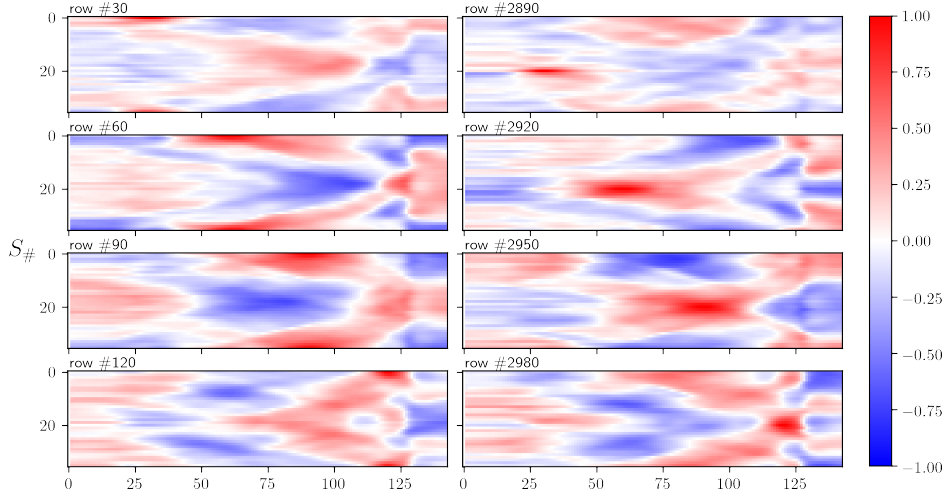


Figure 6: Rows of the (sampled) correlation matrix Γ_{corr} (150 samples) cut up at the points between different wave sources and stacked on top of each other. $S_{\#}$ here means *source number*. Row 2890 corresponds to the same relative time point of the wave as row 30, just for a different source, so it is natural that the second column has structures similar to those in the first column, simply “up-shifted”.

6 Numerical results

Figure 7 illustrates reconstructions of power densities for different boundary conditions (rows 1-3) and the conductivity (row 4). The power densities are reconstructed by solving (4.2) and then the conductivity is found by solving (4.6). Rows 1–3 are power densities corresponding to boundary conditions $f(x_1, x_2) = x_1, x_2, (x_1 + x_2)/\sqrt{2}$ respectively. The first column contains (for comparison) reconstructions of the best possible case with no uncertainty, i.e. the correct sound speed is used for solving the inverse problem.

Looking at columns 2 through 4 in Figure 7, we clearly see the propagation of the model error to the power density, $H(x)$, reconstructions, though, due to the complexity of the error propagation, we remark how the error features have no obvious resemblance to the structures introduced in the sound speed for the data generation; we refer back to Figure 4. A number of these error features seemingly disappear again when moving on to the reconstruction of the conductivity, $\sigma(x)$, though clearly the background variations are notable, and in particular near the boundary we find artifacts. The latter should not be surprising, as the mean sound speed might be slightly different from the constant c_{bg} used in recovery, which, during this study, has been observed to cause structural errors close to the boundary. The inclusion, however, stands out quite clearly, which we attribute to the high and low peaks around the inclusion area present in all the power density reconstructions. Similar encircling high-low peak structures do not appear elsewhere attributing to the non-presence of other inclusions introduced by model errors.

We illustrate in Figure 8 the change in the reconstructed power density relative to the level of difference in sound speed. In the figure progressing from left to right, the scale of the structured variation, controlled by μ , is scaled up. In the left-most reconstruction $\mu = 0$, thus the only error in the sound speed is within the inclusion. The third reconstruction has $\mu = 0.05$ and we note that this is the same reconstruction as row 1–column 2 in Figure 7. This image demonstrates quite nicely the theory developed in the preceding sections. We note that, for the leftmost reconstruction, the used β -parameter was not optimal. The optimal β is very small, and finding it is too computationally expensive without any visual improvement, so a β -value

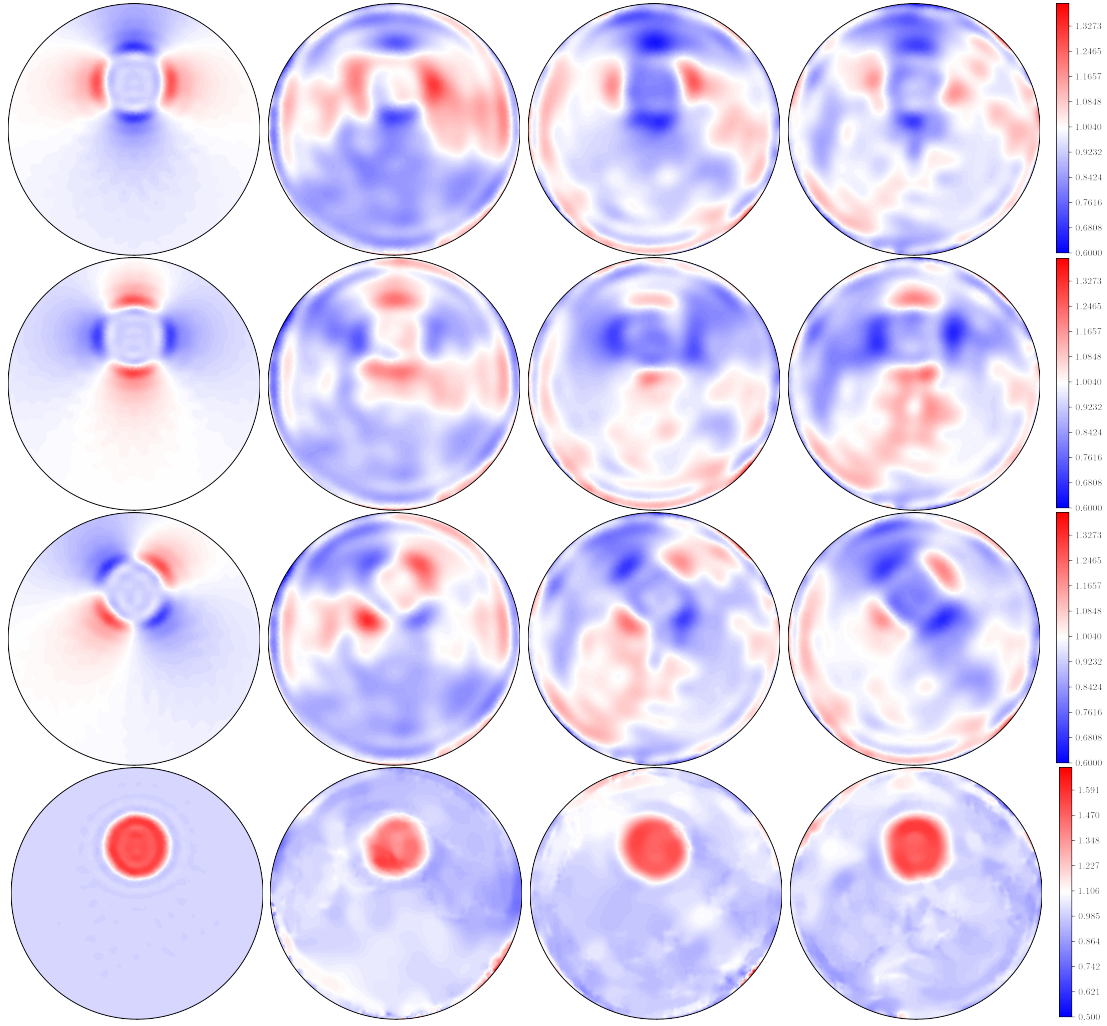


Figure 7: Reconstructions of power densities and conductivities corresponding to different realizations of sound speeds. Rows 1–3 are power densities corresponding to boundary conditions $f(x_1, x_2) = x_1, x_2, (x_1 + x_2)/\sqrt{2}$ respectively. Row 4 is the corresponding reconstructed conductivity from the three power densities above. Column 1 contains the optimal solution with no uncertainty. Columns 2–4 correspond to the particular sound speed realizations shown in Figure 4.

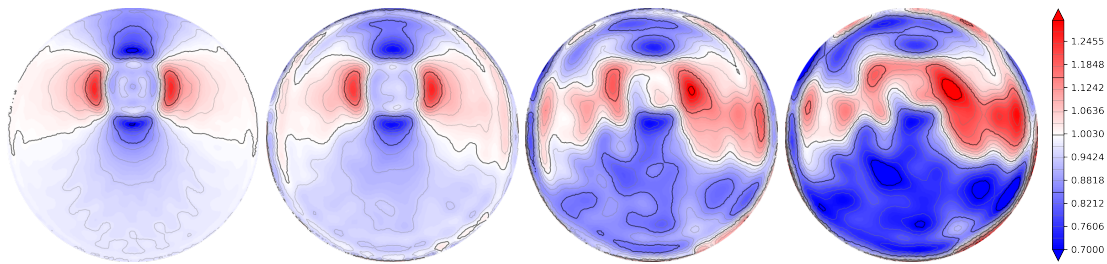


Figure 8: Reconstructions of power densities corresponding to different values of μ . The power density is the one corresponding to the boundary condition $f(x_1, x_2) = x_1$ and the sound speed structure used is the left-most in Figure 4. The values used for μ are (left-to-right) 0.00, 0.01, 0.05 and 0.10.

close to 10^{-8} (where the search algorithm terminated) was used.

We present in Figure 9 the mean and standard deviations, taken point-wise, of the power density and conductivity reconstructions from multiple realization samples. The means illustrate that our sampling does not appear to be biased in promoting non-existing features, which is to be expected but also nice to verify. The standard deviations also highlight some expected features, for example it sky-rockets near the boundary, which is in correspondence with our observations above. This is due to the increasing misalignment between the true wave p and the wave \tilde{p} used for reconstruction as time increases.

In a simplified scenario, if the true sound speed is slightly higher, p will have left the domain before \tilde{p} and the reconstruction algorithm will see no signal as \tilde{p} traverses the last stretch towards the boundary. Thus, the reconstructed power density will exhibit a low-valued zone. On the other hand, if the true sound speed is slightly lower, a reverse phenomenon happens and the reconstructed power density exhibits high values in the area. This phenomenon is very obvious when the error in \tilde{p} is exacerbated by deliberately shifting the used sound speed by some constant.

Also, the boundary of the conductivity inclusion exhibits moderately higher standard deviation, which is not surprising when looking at the conductivity reconstructions in Figure 7; here the inclusion boundary shifts a bit from one to the other. We note that 150 samples were used for computing the means and standard deviations.

7 Discussion and conclusion

As proposed, in this paper we have explored the effect of uncertainty in the wave. In Propositions 3.1 and 3.2 we have established bounds for the deviation of the wave and the operator based on variations in the sound speed coefficient. This guarantees that, for sufficiently small variations in the sound speed, the deviations scale accordingly. Considering how the error in the wave propagates to the operator, we demonstrated in Theorem 4.1 a regularization strategy for model error and used the formerly established propositions to show in Corollary 4.1 the applicability to the AET problem.

In numerical simulations we found that the theory matches observations quite nicely, in particular as illustrated in Figure 8, where we observe directly how the reconstruction improves as the difference between the real and estimated waves decreases. It is of course important to point out that, as mentioned in Remark 4.1, in this study we choose the regularization parameter β in (4.2) optimally. In truth, this is a bit artificial, but it is necessary to be able to compare the different end-result reconstructions. Also, while we do not give the optimal values for β here, for the reconstructions in Figure 8 they start at about 10^{-5} (right-most) and decrease with μ towards zero; the leftmost having an optimal $\beta < 10^{-8}$.

We saw in Figure 7 how the variations in realizations of the sound speed can influence the reconstructed power density quite heavily, propagating the operator error to the reconstruction. It is, however, notable how little of this error continues into the reconstructed conductivity, where the inclusion is quite convincingly reconstructed. We conjecture that this kind of error in the reconstructed power density is not too significant, probably because the features across all the power densities corresponding to the different boundary conditions are not collectively producible by the model $H[\sigma]$ from a single conductivity.

We believe that these results are quite promising for AET showing that, even if the wave is not known exactly, this will not necessarily pose a huge problem for the final recovery of the conductivity, though it might produce irregular and artificial structures in the reconstructed power densities.

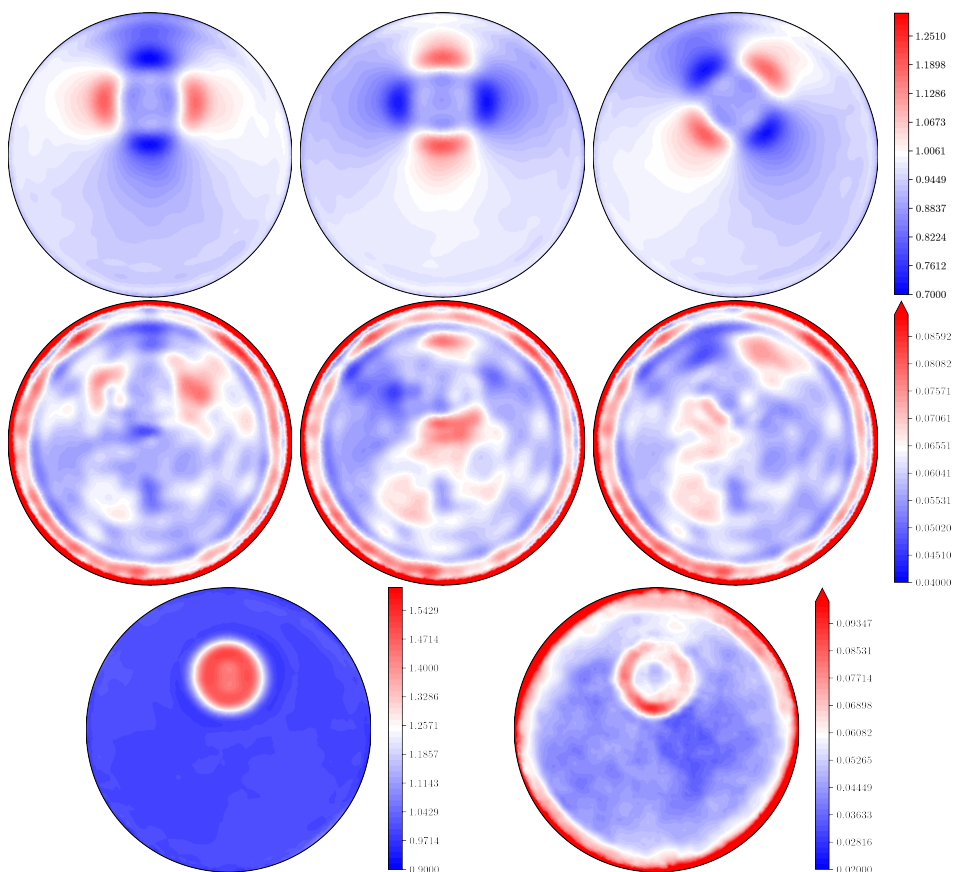


Figure 9: Node-wise means and standard deviations of sampled reconstructions. The upper row contains, left to right, the mean power densities for the boundary conditions $f(x_1, x_2) = x_1$, x_2 , $(x_1 + x_2)/\sqrt{2}$ respectively. The second row contains the corresponding standard deviations, and finally the last row has the mean conductivity on the left and standard deviation on the right. 150 samples were used.

Acknowledgement

KK was supported by The Villum Foundation (grant no. 25893).

References

- [1] R. A. ADAMS AND J. J. FOURNIER, *Sobolev spaces*, vol. 140, Elsevier, 2003.
- [2] B. J. ADESOKAN, B. JENSEN, B. JIN, AND K. KNUDSEN, *Acousto-electric tomography with total variation regularization*, *Inverse Problems*, 35 (2019), pp. 035008, 25.
- [3] B. J. ADESOKAN, K. KNUDSEN, V. P. KRISHNAN, AND S. ROY, *A fully non-linear optimization approach to acousto-electric tomography*, *Inverse Problems*, 34 (2018), pp. 104004, 16.
- [4] G. S. ALBERTI AND Y. CAPDEBOSCQ, *Lectures on elliptic methods for hybrid inverse problems*, vol. 25, Société Mathématique de France, 2018.
- [5] H. AMMARI, E. BONNETIER, Y. CAPDEBOSCQ, M. TANTER, AND M. FINK, *Electrical impedance tomography by elastic deformation*, *SIAM Journal on Applied Mathematics*, 68 (2008), pp. 1557–1573.
- [6] G. BAL, E. BONNETIER, F. MONARD, AND F. TRIKI, *Inverse diffusion from knowledge of power densities*, *Inverse Probl. Imaging*, 7 (2013), pp. 353–375.
- [7] G. BAL, C. GUO, AND F. MONARD, *Imaging of anisotropic conductivities from current densities in two dimensions*, *SIAM J. Imaging Sci.*, 7 (2014), pp. 2538–2557.
- [8] G. BAL, W. NAETAR, O. SCHERZER, AND J. SCHOTLAND, *The Levenberg-Marquardt iteration for numerical inversion of the power density operator*, *J. Inverse Ill-Posed Probl.*, 21 (2013), pp. 265–280.
- [9] R. BARRETT, M. W. BERRY, T. F. CHAN, J. DEMMEL, J. DONATO, J. DONGARRA, V. EIJKHOUT, R. POZO, C. ROMINE, AND H. VAN DER VORST, *Templates for the solution of linear systems: building blocks for iterative methods*, vol. 43, Siam, 1994.
- [10] A.-P. CALDERÓN, *On an inverse boundary value problem*, in *Seminar on Numerical Analysis and its Applications to Continuum Physics (Rio de Janeiro, 1980)*, Soc. Brasil. Mat., Rio de Janeiro, 1980, pp. 65–73.
- [11] Y. CAPDEBOSCQ, J. FEHRENBACH, F. DE GOURNAY, AND O. KAVIAN, *Imaging by modification: Numerical reconstruction of local conductivities from corresponding power density measurements*, *SIAM Journal on Imaging Sciences*, 2 (2009), pp. 1003–1030.
- [12] M. CHENEY, D. ISAACSON, AND J. C. NEWELL, *Electrical impedance tomography*, *Siam Review*, 41 (1999), pp. 85–101.
- [13] L. C. EVANS, *Partial Differential Equations, 2nd edition*, vol. 19, American Mathematical Society, 2010.
- [14] L. HARHANEN, N. HYVÖNEN, H. MAJANDER, AND S. STABOULIS, *Edge-enhancing reconstruction algorithm for three-dimensional electrical impedance tomography*, *SIAM Journal on Scientific Computing*, 37 (2015), pp. B60–B78.
- [15] D. S. HOLDER, *Electrical Impedance Tomography: Methods History and Applications, Series in Medical Physics and Biomedical Engineering*, IOP Press,, 2010.

- [16] S. HUBMER, K. KNUDSEN, C. LI, AND E. SHERINA, *Limited-angle acousto-electrical tomography*, Inverse Problems in Science and Engineering, (2018), pp. 1–20.
- [17] B. JENSEN, A. KIRKEBY, AND K. KNUDSEN, *Feasibility of acousto-electric tomography*, 2019. Preprint in arXiv 1908.04215.
- [18] J. JOSSINET, B. LAVANDIER, AND D. CATHIGNOL, *The phenomenology of acousto-electric interaction signals in aqueous solutions of electrolytes*, Ultrasonics, 36 (1998), pp. 607–613. Ultrasonics International 1997.
- [19] A. KIRSCH, *An introduction to the mathematical theory of inverse problems*, vol. 120 of Applied Mathematical Sciences, Springer-Verlag, New York, 1996.
- [20] P. KUCHMENT AND L. KUNYANSKY, *Synthetic focusing in ultrasound modulated tomography*, Inverse Problems and Imaging, 4 (2010), pp. 665–673.
- [21] ———, *2D and 3D reconstructions in acousto-electric tomography*, Inverse Problems, 27 (2011), p. 055013.
- [22] B. LAVANDIER, J. JOSSINET, AND D. CATHIGNOL, *Experimental measurement of the acousto-electric interaction signal in saline solution*, Ultrasonics, 38 (2000), pp. 929–936.
- [23] C. LI, M. KARAMEHMEDOVIC, E. SHERINA, AND K. KNUDSEN, *Levenberg-Marquardt algorithm for acousto-electric tomography based on the complete electrode model*, 2019. Preprint in arXiv 1912.08085.
- [24] A. LOGG, K.-A. MARDAL, AND G. WELLS, *Automated solution of differential equations by the finite element method: The FEniCS book*, vol. 84, Springer Science & Business Media, 2012.
- [25] F. MONARD AND G. BAL, *Inverse anisotropic diffusion from power density measurements in two dimensions*, Inverse Problems, 28 (2012), pp. 084001, 20.
- [26] L. OKSANEN AND G. UHLMANN, *Photoacoustic and thermoacoustic tomography with an uncertain wave speed*, Mathematical Research Letters, 21 (2014), pp. 1199–1214.
- [27] I. REISER, A. EDWARDS, AND R. NISHIKAWA, *Validation of a power-law noise model for simulating small-scale breast tissue*, Physics in Medicine & Biology, 58 (2013), p. 6011.
- [28] S. ROY AND A. BORZÌ, *A new optimization approach to sparse reconstruction of log-conductivity in acousto-electric tomography*, SIAM J. Imaging Sci., 11 (2018), pp. 1759–1784.
- [29] J. TICK, A. PULKKINEN, AND T. TARVAINEN, *Modelling of errors due to speed of sound variations in photoacoustic tomography using a bayesian framework*, Biomedical Physics & Engineering Express, 6 (2019), p. 015003.
- [30] H. ZHANG AND L. V. WANG, *Acousto-electric tomography*, Progress in Biomedical Optics and Imaging - Proceedings of Spie, 5 (2004), pp. 20, 145–149.